Title	Development of non-equiatomic Ti-Nb-Ta-Zr-Mo high-entropy alloys for metallic biomaterials
Author(s)	Hori, Tetsuya; Nagase, Takeshi; Todai, Mitsuharu et al.
Citation	Scripta Materialia. 2019, 172, p. 83-87
Version Type	VoR
URL	https://hdl.handle.net/11094/89812
rights	This article is licensed under a Creative Commons Attribution 4.0 International License.
Note	

Development of non-equiatomic Ti-Nb-Ta-Zr-Mo high-entropy alloys for metallic biomaterials

Takao Hori [a,1], Takeshi Nagase [a,b,1], Mitsuharu Todai [c], Aira Matsugaki [a], Takayoshi Nakano [a,*]

[a] Division of Materials and Manufacturing Science, Graduate School of Engineering, Osaka University, 2-1 Yamadaoka, Suita, Osaka 565-0871, Japan
[b] Research Center for Ultra-High Voltage Electron Microscopy, Osaka University, 7-1 Mihogaoka, Ibaraki, Osaka 567-0047, Japan
[c] Department of Environmental Materials Engineering, National Institute of Technology, Niihama College, 7-1 Yagumo-cho Niihama, Ehime 792-8580, Japan

ABSTRACT

Nobel non-equiatomic Ti-Nb-Ta-Zr-Mo high-entropy alloys (HEAs) for metallic biomaterials (bio-HEAs) were designed and developed. The pseudo-binary phase diagrams focusing on solidification were constructed by thermodynamic calculations. The shifting the alloy composition of the equiatomic TiNbTaZrMo bio-HEA can realize the drastic improvement of the deformability. Notably, the non-equiatomic Ti, Zr-rich composition stimulated the molecular interaction between biological cells and bio-HEA, indicating the possibility of the proposed non-equiatomic Ti-Nb-Ta-Zr-Mo HEAs as an advanced biomaterial for bone tissue engineering applications. This is the first achievement for the alloy design including the control of alloy composition for the development of new bio-HEAs.

© 2019 Acta Materialia Inc. Published by Elsevier Ltd. This is an open access article under the CC BY license (http://creativecommons.org/licenses/by/4.0/).

A new generation of metallic biomaterials that exhibit both biocompatibility and suitable mechanical properties are urgently required to meet future demands of the medical field. Recently, a new class of structural materials called high-entropy alloys (HEAs) was developed [1–7]. An equiatomic TiNbTaZrMo HEA was first developed as an HEA for metallic biomaterials [8–11]. In this paper, HEAs for metallic biomaterials are denoted as bio-HEAs. The equiatomic TiNbTaZrMo bio-HEA showed superior biocompatibility compared to CP-Ti, and its mechanical strength was superior to that of a Ti-6Al-4V alloy [8]. The equiatomic TiNbTaZrMo bio-HEA showed the high corrosion resistance under isotonic sodium chloride solution at 310 K [9]. The application of this equiatomic TiNbTaZrMo bio-HEA for orthopedic implants was investigated by Wang and Xu [11]. A non-equiatomic $Ti_{2.6}$NbTaZrMo bio-HEA with a liquidus temperature T_L lower than that of the equiatomic TiNbTaZrMo bio-HEA, was developed based on thermodynamic calculations focusing on solidification [10]. The constituent elements of these bio-HEAs were mainly Group IV elements (Ti, Zr, and Hf), Group V elements (Nb and Ta), and Group VI elements (Cr and Mo), and the alloys were similar to refractory high-entropy alloys (RHEAs) [12–16]. A number of RHEAs have been developed to date [16], whereas the development of bio-HEAs is strictly restricted because of the severe limitations of the constituent elements in terms of biocompatibility. In this study, non-equiatomic Ti-Nb-Ta-Zr-Mo bio-HEAs were designed and fabricated.

The constituent elements in bio-HEAs are similar to those in RHEAs; however, the concepts of alloy design and desired mechanical and functional properties are significantly different between bio-HEAs and RHEAs [8–10]. In bio-HEAs, the biocompatibility of the constituent elements is the most important parameter for alloy design. The mechanical properties in the high-temperature region are not important for bio-HEAs, although room-temperature strength and ductility are important factors. The high liquidus temperature (T_L) may be favorable for RHEAs, but such properties are not commonly exhibited by bio-HEAs. A significantly high T_L restricts the fabrication of bio-HEAs and increases the fabrication cost. A low T_L can overcome the limitations of the fabrication and enable significantly more cost-effective production of bio-HEAs. Therefore, a low T_L is preferred in the development of novel bio-HEAs from the viewpoint of materials engineering and manufacturing of metallic biomaterials. In the present study, $Ti_{2-x}Zr_{2-x}Nb_xTa_xMo_x$ and $Ti_{2-y}ZrNbTaMo_y$ bio-HEAs were designed as non-equiatomic Ti-Nb-Ta-Zr-Mo bio-HEAs based on the following four concepts: (1) alloys whose mixing entropy (ΔS_{mix}) was 1.5R and above were designed to satisfy the entropy-based definition for the HEAs [5,6]; (2) the constituent elements were Ti, Nb, Ta, Zr, and Mo, and additional elements were not included because this combination of elements exhibited superior biocompatibility; (3) a decrease in T_L, for ease of fabrication; and (4) a decrease in the number of total electrons based on the valence electron concentration (VEC) theory for room-temperature ductility [17,18]. Concerning the alloy design concept (concept 2), an earlier study on thermodynamic calculations focusing on the solidification in Ti-Nb-Ta-Zr-Mo bio-HEAs [9,10,19] clarified that an increase in the value of z in Ti_zNbTaZrMo ($z \geq 1$) and TiNbTaZr$_z$Mo ($z \geq 1$) alloys and a decrease in

the value of z in $TiNbTa_zZrMo$ ($z \leq 1$) and $TiNbTaZrMo_z$ ($z \leq 1$) alloys were effective in decreasing the T_L. This implies that an increase in (Ti + Zr) and/or a decrease in (Ta + Mo) leads to a decrease in T_L. From the viewpoint of the alloy design concept (concept 4) on room-temperature ductility, Sheikh et al. reported that a decrease in the number of valence electrons (s + d electrons) through controlled alloying, based on the application of the VEC theory in HEAs [17], was effective in intrinsically ductilizing RHEAs [18]. Based on the relationship between VEC and room-temperature ductility in RHEAs [18], an increase in Ti (VEC = 4) and Zr (VEC = 4) was considered to be effective in ductilizing bio-HEAs, whereas an increase in Mo (VEC = 6) did not improve the room-temperature ductility of the bio-HEAs. To decrease T_L and enhance room-temperature ductility simultaneously, an increase in the concentration of Ti and Zr and a decrease in the concentration of Nb, Ta, and Mo from the equiatomic TiNbTaZrMo were designed, resulting in the $Ti_{2-x}Zr_{2-x}Nb_xTa_xMo_x$ bio-HEAs. $Ti_{2-y}ZrNbTaMo_y$ bio-HEAs were also designed based on the concepts of increasing the Ti concentration and decreasing the Mo concentration from the equiatomic TiNbTaZrMo.

Pseudo-binary phase diagrams constructed using only the Gibbs free energies of a single liquid phase and a single body-centered cubic (BCC) T_L and the solidus temperature (T_S) and in predicting the solidification microstructure in the Ti-Nb-Ta-Zr-Mo bio-HEAs [9,10,19]. Fig. 1 shows the pseudo-binary phase diagrams, focusing on T_L [K] and T_S [K], which were estimated from thermodynamic calculations focusing on solidification. The thermodynamic calculations were performed with FactSage (ver. 7.2) using the thermodynamic databases for alloy systems from the Scientific Group Thermodata Europe (SGTE) 2017 [20].
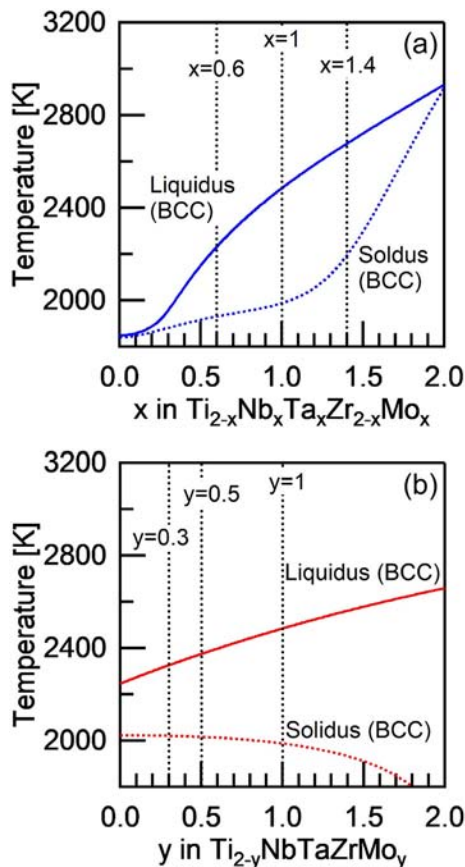

Fig. 1. Pseudo-binary phase diagrams focusing on liquidus temperature T_L [K] and solidus temperature T_S [K], estimated from thermodynamic calculations considering a single liquid phase and a single BCC phase: (a) $Ti_{2-x}Zr_{2-x}Nb_xTa_xMo_x$ and (b) $Ti_{2-y}ZrNbTaMo_y$. T_L and T_S are shown as a red solid line and a red broken line, respectively.

In the pseudo-binary phase diagram of $Ti_{2-x}Zr_{2-x}Nb_xTa_xMo_x$ focusing on the solidification of the BCC phase (Fig. 1a), T_L and T_S monotonically increased with increasing x, i.e., T_L and T_S decreased with increasing Ti and Zr concentrations in the $Ti_{2-x}Zr_{2-x}Nb_xTa_xMo_x$ bio-HEAs. For the $Ti_{2-y}ZrNbTaMo_y$ bio-HEAs (Fig. 1b), T_L and T_S also decreased with increasing y. The increase in the Ti concentration and decrease in the Mo concentration were effective in decreasing the T_L and T_S values of the $Ti_{2-y}ZrNbTaMo_y$ bio-HEAs. Based on the thermodynamic calculation results (Fig. 1) and the empirical alloy parameters for the solid solution formation tendency in multicomponent alloys [21], $Ti_{2-x}Zr_{2-x}Nb_xTa_xMo_x$ ($x = 0.6$) and $Ti_{2-y}ZrNbTaMo_y$ ($y = 0.5$, $y = 0.3$) bio-HEAs were designed. As a reference, a Ti-Zr-poor $Ti_{2-x}Zr_{2-x}Nb_xTa_xMo_x$ ($x = 1.4$) bio-HEAs was also designed. The T_L values of the Ti-Zr–rich $Ti_{1.4}Zr_{1.4}Nb_{0.6}Ta_{0.6}Mo_{0.6}$ (2232K), Ti-rich $Ti_{1.7}ZrNbTaMo_{0.3}$ (2374 K), and $Ti_{1.5}ZrNbTaMo_{0.5}$ (2325 K) alloys were much lower than that of the equiatomic TiNbTaZrMo (2484 K) bio-HEA. In contrast, the T_L value of the Ti-Zr–poor $Ti_{0.6}Zr_{0.6}Nb_{1.4}Ta_{1.4}Mo_{1.4}$ (2676 K) was higher than that of the equiatomic TiNbTaZrMo bio-HEA.

Arc-melted ingots of equiatomic TiNbTaZrMo and non-equiatomic $Ti_{2-x}Zr_{2-x}Nb_xTa_xMo_x$ ($x = 0.6$, 1.4) and $Ti_{2-y}ZrNbTaMo_y$ ($y = 0.3$, 0.5) bio-HEAs were prepared by mixing lumps of the pure elements. The purity of the Ti, Nb, Ta, Zr, and Mo resources was above 3 N (99.9%). To achieve a homogeneous distribution of the constituent elements in the alloys, the alloys were melted >10 times and maintained in a liquid state for approximately 120 s during each melting event. The cooling rates during arc melting were roughly estimated to be on the order of 2×10^3 Ks^{-1} [9,22]. The microstructure and constituent phases of the ingots were investigated by X-ray diffraction (XRD) analysis, scanning electron microscopy (SEM), and electron probe microanalysis (EPMA). Rectangular specimens for compression testing, with dimensions of approximately 2 mm × 2 mm × 5 mm, were cut from the ingots using an electron discharge machine. The compression tests were conducted using an Instron-type testing machine at a nominal strain rate of 1.67 × 10^{-4} s^{-1} at room temperature. To evaluate the biocompatibility, the specimens for the cell culture experiment were cut into $\phi = 9$ mm × 1 mm samples using an electron discharge machine. The surfaces of these specimens were mechanically polished using SiC waterproof papers up to 4000 grit and a diamond paste. Prior to the cell culture experiment, the specimens were cleaned using acetone and ethanol by ultrasonication and then placed individually into a 48-well plate ($n = 5$). Primary osteoblasts were isolated from neonatal mice calvariae by sequential collagenase/trypsin digestion. The obtained cells were diluted to 6000 cells/cm^2 and seeded onto the specimens. After culturing for 24 h in a 5% CO$_2$ humidified atmosphere, the cells were fixed with methanol and stained with a 5% Giemsa aqueous solution. The cell density was evaluated using optical microscopy images. The cell adhesion behaviors were evaluated using immunocytochemistry. After culturing for 24 h, the cells were fixed in 4% paraformaldehyde, washed in phosphate-buffered saline with Triton X-100 and immersed in 1% normal goat serum. Then, the cells were incubated with anti-vinculin antibodies (Sigma), followed by incubation in secondary antibodies (Alexa Fluor 594-goat anti-mouse IgG, Thermo Fisher Scientific) and Alexa Fluor 488-phalloidin (Thermo Fisher Scientific). Focal adhesions were analyzed using CellProfiler software (Broad Institute). The data are expressed as mean ± standard deviation. The statistical significance was assessed using one-way ANOVA, followed by Tukey's post-hoc test. A significance of $P < 0.05$ was required for rejection of the null hypothesis.

Fig. 2 shows solidification microstructure analysis results of the ingots. In the XRD patterns (Fig. 2a), the peaks were indexed as BCC solid solutions: the formation of a dual-BCC phase composed of a BCC-1 phase (indicated by the index ●) and a BCC-2 phase (indicated by the index ○) was observed in the equiatomic TiNbTaZrMo bio-HEA. In this study, the BCC-1 (●) and BCC-2 (○) phases were defined as follows: the peak positions at 2θ of BCC-1 were higher than those of BCC-2. An apparent disassociation of the peaks and/or the appearance
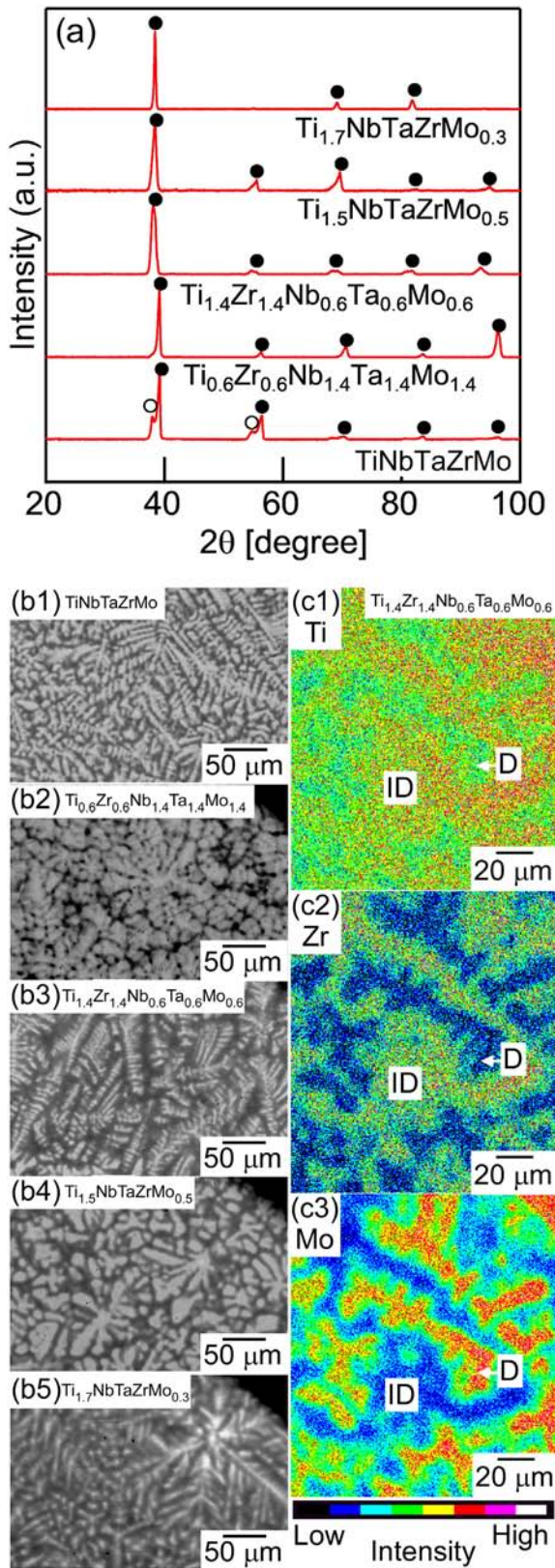
intermetallic compounds and/or BCC-based ordering structures were observed in the XRD patterns. Fig. 2b shows the SEM–back scattering electron (BSE) images of the ingots. An equiaxed dendrite structure composed of a light-gray-contrast dendrite and a dark-gray-contrast inter-dendrite was observed, regardless of the alloy composition. The ratio of the inter-dendrite region (dark-gray contrast)/dendrite region (light-gray contrast) in the $Ti_{2-x}Zr_{2-x}Nb_xTa_xMo_x$ ($x = 0.6, 1.0, 1.4$) bio-HEAs showed a tendency to increase with increasing Ti and Zr ratio. To clarify the elemental distribution of the constituent elements in the ingots, EPMA-wavelength dispersive X-ray spectroscopy (WDS) analysis was performed. Fig. 2c shows the elemental map of the ingots of the non-equiatomic $Ti_{1.4}Zr_{1.4}Nb_{0.6}Ta_{0.6}Mo_{0.6}$ bio-HEA as a typical example. Ti and Zr show a tendency to be enriched in the main dendrite region (D) rather than in the inter-dendrite region (ID) (Fig. 2c1, c2), whereas Mo shows the opposite tendency (Fig. 2c3). The thermodynamic calculation of the distribution coefficient at T_L of Ti, Zr, and Mo in the $Ti_{1.4}Zr_{1.4}Nb_{0.6}Ta_{0.6}Mo_{0.6}$ bio-HEA was 0.60, 0.28, and 1.81, respectively. The correspondence between the Ti and Zr enrichment in the ID and the thermodynamic calculation results of the distribution coefficient indicated the accuracy for the thermodynamic calculation focusing on the solidification shown in Fig. 1. The XRD, SEM, and EPMA analyses (Fig. 2) indicate the formation of a BCC phase without intermetallic compounds in the ingots of the non-equiatomic $Ti_{2-x}Zr_{2-x}Nb_xTa_xMo_x$ ($x = 0.6, 1.4$) and $Ti_{2-y}ZrNbTaMo_y$ ($y = 0.3, 0.5$) bio-HEAs.

Fig. 3 shows the mechanical property analysis results of the room-temperature engineered stress versus plastic strain curves of the ingots of the non-equiatomic $Ti_{2-x}Zr_{2-x}Nb_xTa_xMo_x$ ($x = 0.6, 1.4$) and $Ti_{2-y}ZrNbTaMo_y$ ($y = 0.3, 0.5$) bio-HEAs, together with that of the equiatomic TiNbTaZrMo bio-HEA. The 0.2% proof stress ($\sigma_{0.2}$) in the non-equiatomic Ti-Nb-Ta-Zr-Mo bio-HEAs was slightly lower than that in the equiatomic Ti-Nb-Ta-Zr-Mo bio-HEA; however, the values of $\sigma_{0.2}$ were still quite high, over 1000 MPa. It should be noted that the fracture strains in the ingots of the $Ti_{1.4}Zr_{1.4}Nb_{0.6}Ta_{0.6}Mo_{0.6}$ (Fig. 3a), $Ti_{1.7}ZrNbTaMo_{0.3}$, and $Ti_{1.5}ZrNbTaMo_{0.5}$ (Fig. 3b) bio-HEAs

Fig. 2. Solidification microstructure analysis results of the ingots of bio-HEAs: (a) XRD patterns, (b) SEM-BSE images, (c) EPMA-WDS elemental mapping of $Ti_{1.4}Zr_{1.4}Nb_{0.6}Ta_{0.6}Mo_{0.6}$.

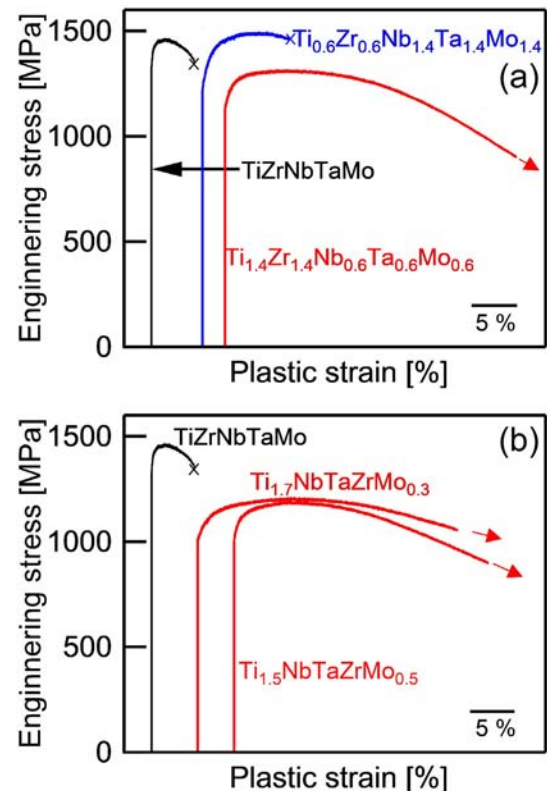**Fig. 3.** Mechanical properties of the ingots of bio-HEAs: (a) TiNbTaZrMo and $Ti_{2-x}Zr_{2-x}Nb_xTa_xMo_x$ and (b) TiNbTaZrMo and $Ti_{2-y}ZrNbTaMo_y$.

of shoulder peaks of the BCC phase were not observed in the ingots of the non-equiatomic $Ti_{2-x}Zr_{2-x}Nb_xTa_xMo_x$ ($x = 0.6, 1.4$) and $Ti_{2-y}ZrNbTaMo_y$ ($y = 0.5, 0.3$) bio-HEAs. No peaks corresponding to

were much higher than those in the equiatomic TiNbTaZrMo and $Ti_{0.6}Zr_{0.6}Nb_{1.4}Ta_{1.4}Mo_{1.4}$ bio-HEAs (Fig. 3a). The compression deformability of the ingots was drastically modified by increasing the Ti and Zr concentration and/or decreasing the Mo concentration in the Ti-Nb-Ta-Zr-Mo bio-HEAs.

Fig. 4 shows the biocompatibility evaluation results of the ingots. In the Giemsa staining images of osteoblasts on the ingots (Fig. 4a), the osteoblasts cultured for 24 h on stainless steel (SUS-316L) (Fig. 4a1 and a4) and CP-Ti (Fig. 4a2) appeared as typical metallic biomaterials, and the $Ti_{1.4}Zr_{1.4}Nb_{0.6}Ta_{0.6}Mo_{0.6}$ (Fig. 4a3 and a5) bio-HEA appeared as a typical non-equiatomic Ti-Nb-Ta-Zr-Mo bio-HEA whose T_L was the lowest among the non-equiatomic Ti-Nb-Ta-Zr-Mo bio-HEAs. A significant difference in the cell density between CP-Ti (Fig. 4a2) and the $Ti_{1.4}Zr_{1.4}Nb_{0.6}Ta_{0.6}Mo_{0.6}$ bio-HEA (Fig. 4a3) was not observed. The morphology of osteoblasts on biomaterials is an important indicator, along with the cell density. Fig. 4a4 and a5 are magnified images of the morphology of the osteoblasts. Cell spreading controls cellular functions involving gene expression, migration, and intercellular communication. The osteoblasts on SUS-316L showed a relatively small, less widespread morphology (Fig. 4a4). In contrast, the osteoblasts on the $Ti_{1.4}Zr_{1.4}Nb_{0.6}Ta_{0.6}Mo_{0.6}$ bio-HEA showed a widespread morphology (Fig. 4a5), which was quite similar to that of the cells on CP-Ti and equiatomic TiNbTaZrMo [8]. Fig. 4b shows fluorescent images of osteoblast adhesion on the fabricated specimens. The insets show the enlarged images of the typical focal adhesions. The white arrows indicated by the index P show that small round focal adhesions formed on SUS316L (Fig. 4b1), CP-Ti (Fig. 4b2), equiatomic TiNbTaZrMo (Fig. 4b3), and $Ti_{0.6}Zr_{0.6}Nb_{1.6}Ta_{1.4}Mo_{1.4}$ (Fig. 4b4). In contrast, the yellow arrows indicated by the index Q in $Ti_{1.4}Zr_{1.4}Nb_{0.6}Ta_{0.6}Mo_{0.6}$ (Fig. 4b5) show the formation of elongated mature focal adhesions (fibrillar adhesions). Fig. 4c shows the quantitative analysis of size regulation of fibrillar adhesions (longer than 5 μm) in osteoblasts cultured on the fabricated specimens. The number inside the circle indicates the amount of fibrillar adhesion ($\times 10/mm^2$). The osteoblasts adhered on the bio-HEAs expressed relatively higher amounts of fibrillar adhesion compared to SUS316L. In addition, the cells on the $Ti_{1.4}Zr_{1.4}Nb_{0.6}Ta_{0.6}Mo_{0.6}$ bio-HEAs possessed significantly longer structures of fibrillar adhesion compared to the $Ti_{0.6}Zr_{0.6}Nb_{1.4}Ta_{1.4}Mo_{1.4}$ bio-HEA, indicating that the $Ti_{1.4}Zr_{1.4}Nb_{0.6}Ta_{0.6}Mo_{0.6}$ bio-HEA stimulated the maturation of focal adhesion plaques in the osteoblasts. The maturation of focal adhesion, as well as cell alignment, is closely related to the functional organization of biological tissue around the implanted biomaterials [23-25]. The maturation of focal adhesion is closely related to the functional organization of biological tissue around the implanted biomaterials [23]. These results demonstrate the superior biocompatibility of the non-equiatomic $Ti_{1.4}Zr_{1.4}Nb_{0.6}Ta_{0.6}Mo_{0.6}$ bio-HEA as compared to that of SUS316L; the biocompatibility could be modified by controlling the alloy compositions in the Ti-Nb-Ta-Zr-Mo bio-HEAs.

In conclusion, non-equiatomic Ti-Nb-Ta-Zr-Mo bio-HEAs of $Ti_{2-x}Zr_{2-x}Nb_xTa_xMo_x$ ($x = 0.6$) and $Ti_{2-y}ZrNbTaMo_y$ ($y = 0.3, 0.5$) were designed. Pseudo-binary phase diagrams focusing on the liquidus and solidus of the BCC phase (Fig. 1) were constructed for these bio-HEAs by thermodynamic calculations for the alloy design. The solidification microstructure (Fig. 2), mechanical properties (Fig. 3), and biocompatibility (Fig. 4) of the $Ti_{2-x}Zr_{2-x}Nb_xTa_xMo_x$ and $Ti_{2-y}ZrNbTaMo_y$ bio-HEAs were clarified. The obtained results are summarized as follows:

(1) The thermodynamic calculations indicated that a decrease in x in $Ti_{2-x}Zr_{2-x}Nb_xTa_xMo_x$ and a decrease in y in the $Ti_{2-y}ZrNbTaMo_y$ bio-HEAs led to a decrease in T_L.

(2) An equiaxed dendrite structure with a BCC structure was observed in the ingots of the $Ti_{2-x}Zr_{2-x}Nb_xTa_xMo_x$ and $Ti_{2-y}ZrNbTaMo_y$ bio-HEAs.

(3) The room-temperature deformability of the non-equiatomic Ti-Nb-Ta-Zr-Mo bio-HEAs of $Ti_{2-x}Zr_{2-x}Nb_xTa_xMo_x$ ($x = 0.6$) and $Ti_{2-y}ZrNbTaMo_y$ ($y = 0.3, 0.5$) was much higher than that of
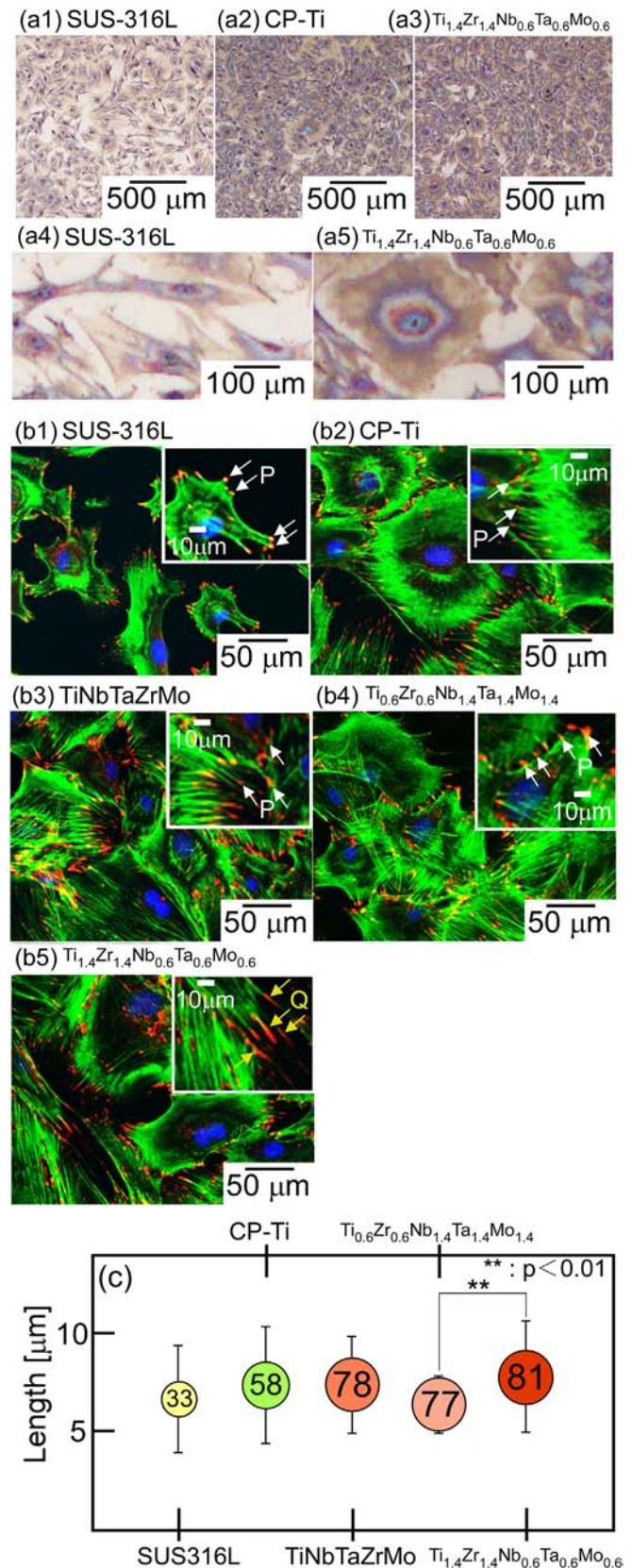

Fig. 4. Biocompatibility of the ingots of bio-HEAs. (a) Giemsa staining images of osteoblasts on the fabricated specimens of SUS316L (stainless steel), CP-Ti (commercial pure titanium), and $Ti_{1.4}Zr_{1.4}Nb_{0.6}Ta_{0.6}Mo_{0.6}$, (b) fluorescent images of osteoblast adhesion on the fabricated specimens of SUS316, CP-Ti, equiatomic TiNbTaZrMo, and non-equiatomic $Ti_{2-x}Zr_{2-x}Nb_xTa_xMo_x$ ($x = 0.6, 1.4$) bio-HEAs, and (c) quantitative analysis of size regulation of fibrillar adhesions (longer than 5 μm) in osteoblasts cultured on the fabricated specimens.

the equiatomic TiNbTaZrMo bio-HEA.

(4) The osteoblasts adhered onto the bio-HEAs expressed relatively higher amounts of fibrillar adhesion compared to SUS316L. The $Ti_{1.4}Zr_{1.4}Nb_{0.6}Ta_{0.6}Mo_{0.6}$ bio-HEAs possessed significantly longer structures of fibrillar adhesion compared to $Ti_{0.6}Zr_{0.6}Nb_{1.4}Ta_{1.4}Mo_{1.4}$ bio-HEA. These results demonstrated the superior biocompatibility of the non-equiatomic $Ti_{1.4}Zr_{1.4}Nb_{0.6}Ta_{0.6}Mo_{0.6}$ bio-HEA.

Acknowledgments

References

[1] B. Cantor, I.T.H. Chang, P. Knight, A.J.B. Vincent, Mater. Sci. Eng. A 375-377 (2004) 213–218.
[2] J.W. Yeh, S.K. Chen, S.J. Lin, J.Y. Gan, T.S. Chin, T.T. Shun, C.H. Tsau, S.Y. Chang, Adv. Eng. Mater. 6 (2004) 299–303.
[3] S. Ranganathan, Curr. Sci. 85 (2003) 1404–1406.
[4] Y. Zhang, Y.J. Zhou, J.P. Lin, G.L. Chen, P.K. Liew, Adv. Eng. Mater. 10 (2008) 534–538.
[5] B.S. Murty, J.-W. Yeh, S. Ranganathan, High-entropy Alloys, first ed Elsevier, 2014.
[6] M.C. Gao, J.-W. Yeh, P.K. Liew, Y. Zhang, High-entropy Alloys, Fundamentals and Applications, first ed., Springer, 2016.
[7] W. Zhang, P.K. Liew, Y. Zhang, Sci. China Mater. 61 (2018) 2–22.
[8] M. Todai, T. Nagase, T. Hori, A. Matsugaki, A. Sekita, T. Nakano, Scr. Mater. 129 (2017) 65–68.
[9] T. Nagase, K. Mizuuchi, T. Nakano, Entropy 21 (483) (2019) 1–17.
[10] T. Nagase, M. Todai, T. Hori, T. Nakano, J. Alloy. Compd. 753 (2018) 412–421.
[11] S.P. Wang, J. Xu, Mater. Sci. Eng. C73 (2017) 80–89.
[12] O.N. Senkov, G.B. Wilks, D.B. Miracle, C.P. Chuang, P.K. Liaw, Intermetallics 18 (2010) 1758–1765.
[13] O.N. Senkov, G.B. Wilks, J.M. Scott, D.B. Miracle, Intermetallics 19 (2011) 698–706.
[14] O.N. Senkov, J.M. Scotta, S.V. Senkova, D.B. Miracle, C.F. Woodward, J. Alloy. Compd. 509 (2011) 6043–6048.
[15] O.N. Senkov, J.M. Scott, S.V. Senkova, F. Meisenkothen, D.B. Miracle, C.F. Woodward, J. Mater. Sci. 47 (2012) 4062–4074.
[16] O.N. Senkov, D.B. Miracle, K.J. Chaput, J.-P. Couzinie, J. Mater. Res. 33 (2018) 3092–3128.
[17] S. Guo, C. Ng, J. Lu, C.T. Liu, J. Appl. Phys. 109 (103505) (2011) 1–6.
[18] S. Sheikh, S. Shafeie, Q. Hu, J. Ahlstrom, C. Persson, J. Vesely, J. Zyka, U. Klement, S. Guo, J. Appl. Phys. 120 (164902) (2016) 1–5.
[19] T. Nagase, K. Mizuuchi, M. Todai, T. Nakano, Materia Japan 58 (2019) 78.
[20] C.W. Bale, A.D. Pelton, W.T. Thompson, G. Eriksson, FactSage, Ecole Poly-technique, Montreal, 2001http://www.crct.polymtl.ca, Accessed date: 21 April 2016.
[21] T. Nagase, T. Hori, M. Todai, A. Matsugaki, T. Nakano, in preparation.
[22] T. Nagase, M. Matsumoto, Y. Fujii, J. of Alloys and Compounds 738 (2018) 440–447.
[23] Y. Nakanishi, A. Matsugaki, K. Kawahara, T. Ninomiya, H. Sawada, T. Nakano, Biomaterials 209 (2019) 103–110.
[24] A. Matsugaki, G. Aramoto, T. Ninomiya, H. Sawada, S. Hata, T. Nakano, Biomaterials 37 (2015) 134–143.
[25] A. Matsugaki, N. Fujiwara, T. Nakano, Acta Biomater. 9 (2013) 7227–7235.